Supplementary Information (SI) for Energy & Environmental Science.
This journal is © The Royal Society of Chemistry 2024

Electronic Supplementary Material (ESI) for Energy & Environmental Science

Field-Responsive Grain Boundary Against Dendrite Penetration for All-Solid-State Batteries

Bing-Qing Xiong[a], Xiaoye Liu [a], Qingshun Nian[a], Zihong Wang [a], Yuhong Zhu[a], Xuan Luo[a], Jinyu Jiang[a], Digen Ruan[a], Jun Ma[a], Junhao Jiang[a], Yi-Feng Cheng[b], Changhao Li[b], Xiaodi Ren*[a]

a. Hefei National Research Center for Physical Science at the Microscale, Department of Materials Science and Engineering, University of Science and Technology of China, Anhui 230026, China

b. State Grid Anhui Electric Power Research Institute, State Grid Laboratory of Fire Protection for Transmission and Distribution Facilities, Anhui Province Key Laboratory of Electric Fire and Safety Protection, Hefei 230601, China

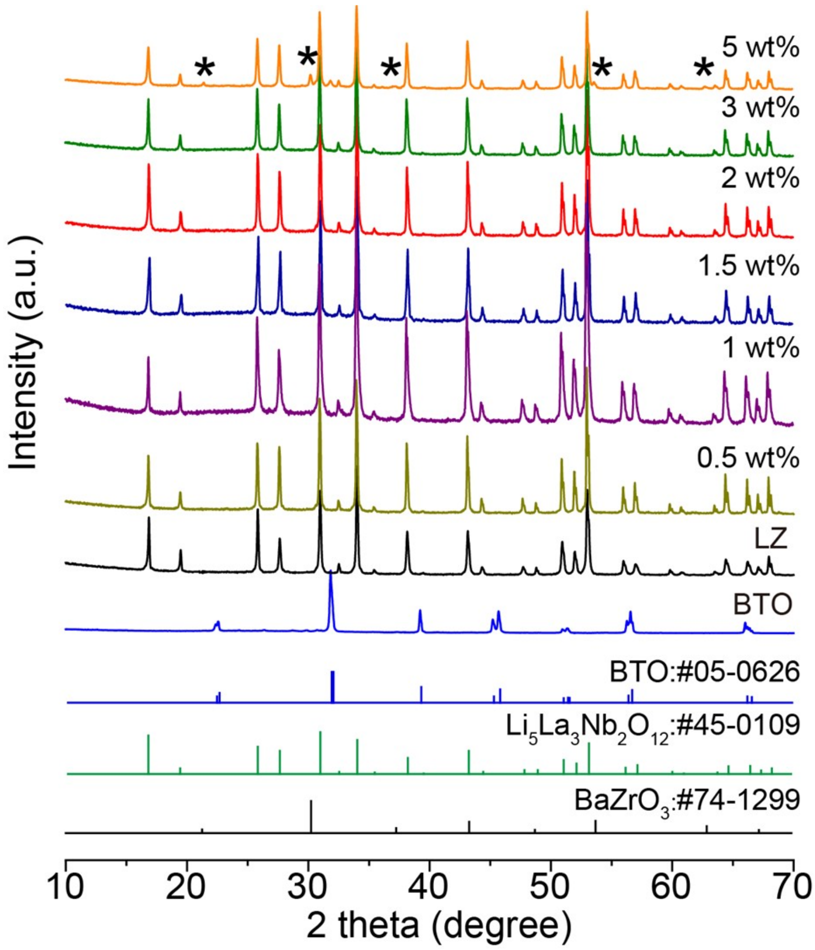

Fig. S1. XRD patterns of BTO-LZ with different weights of BTO.

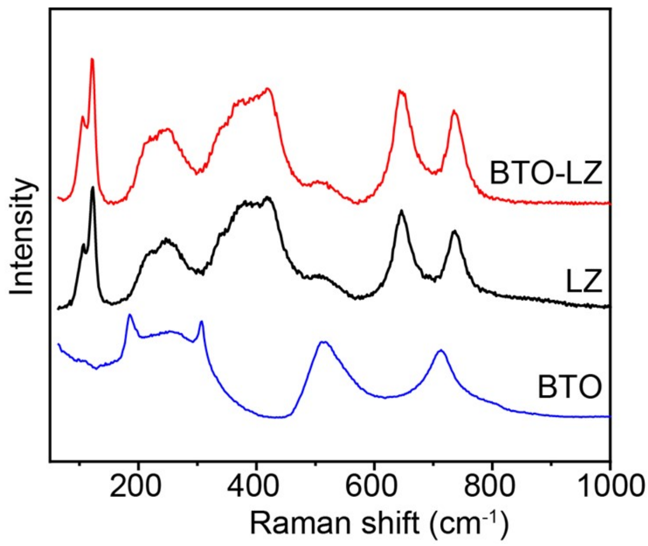

Fig. S2. Raman spectra of BTO, LZ and BTO-LZ.

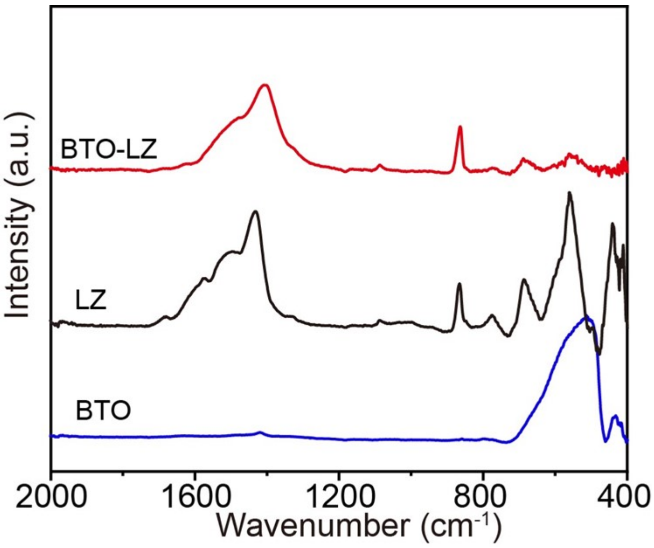

Fig. S3. FT-IR spectra of BTO, LZ and BTO-LZ.

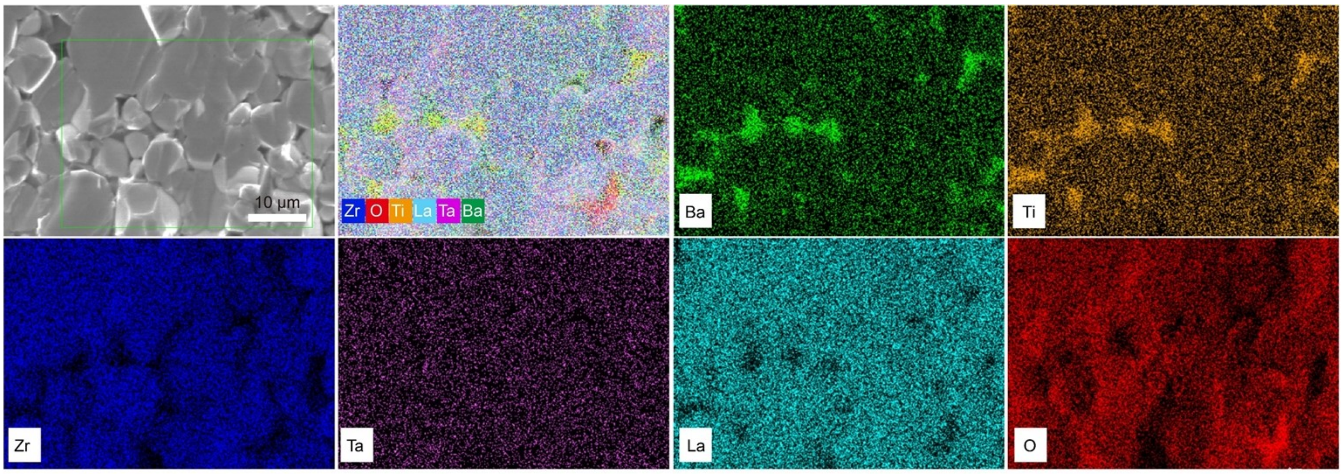

Fig. S4. Cross-sectional SEM images and EDS-mapping of BTO-LZ pellets (samples were prepared by breaking the sintered SSE disc).

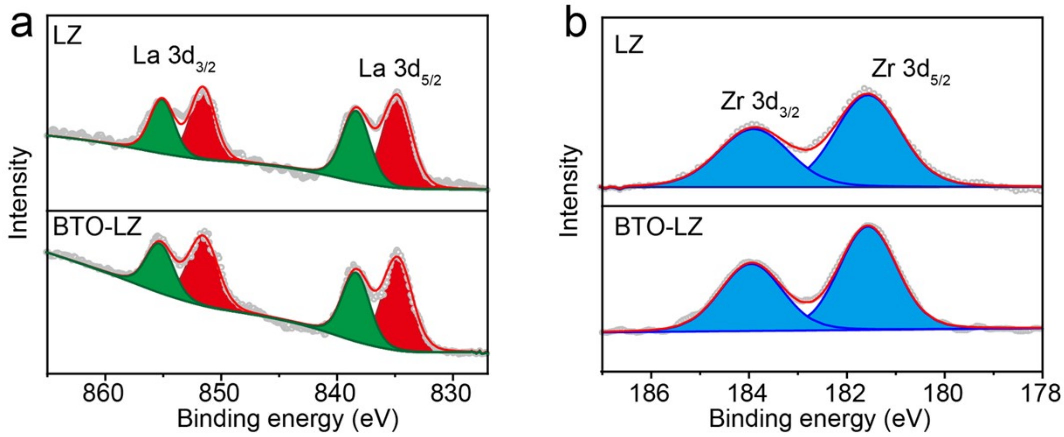

Fig. S5. XPS spectra of (a) La 3d and (b) Zr 3d of LZ and BTO-LZ.

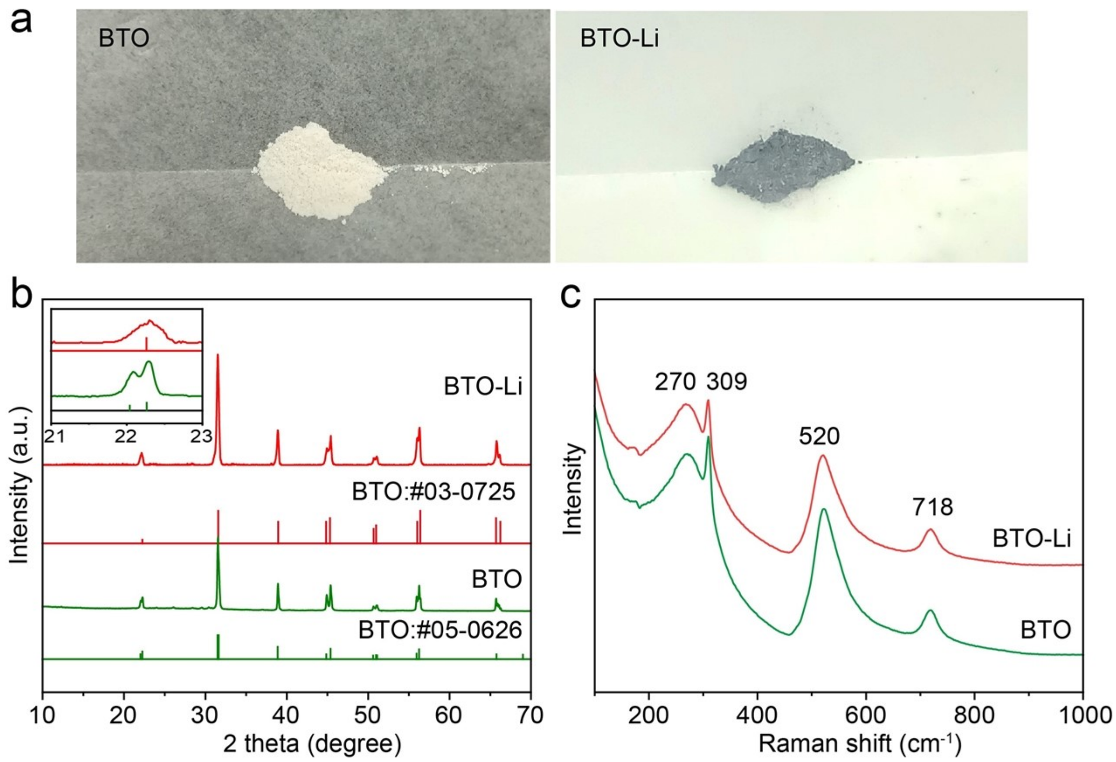

Fig. S6. (a) Optical photos, (b) XRD patterns and (c) Raman spectra of BTO powder and BTO-Li.

Note: To better observe the phenomena of this reaction, BTO ceramics were first ground to a powder and then allowed to react with molten lithium for 20 minutes.

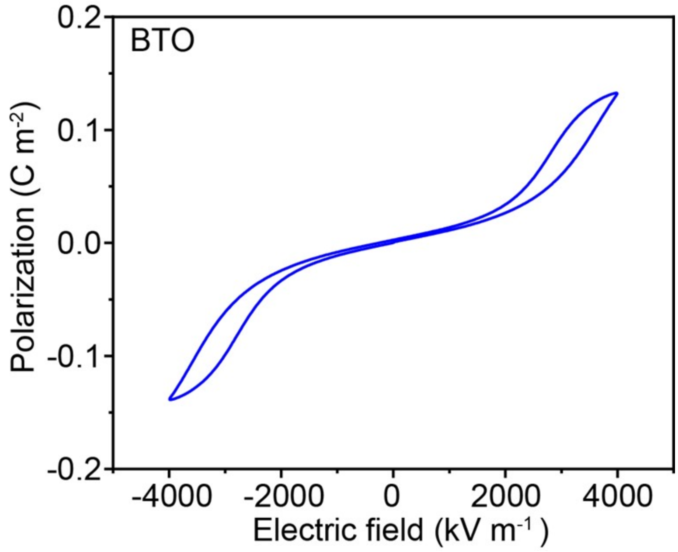

Fig. S7. Polarization-electric field hysteresis loop of the commercial BTO ceramics.

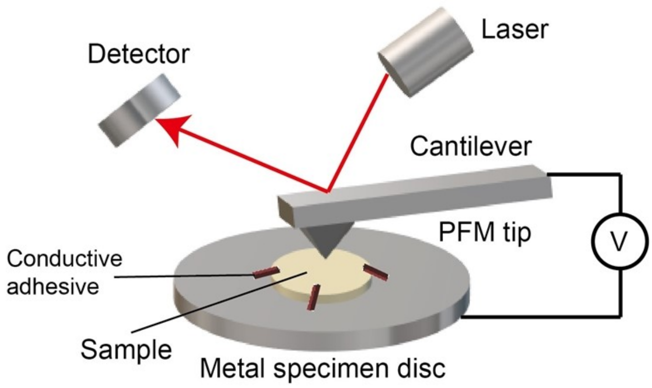

Fig. S8. Schematic representation of the PFM measurement setup.

Note: Fig. S8 shows the piezoresponse force microscopy (PFM) setup used in the ferroelectric response test. PFM enables the assessment of ferroelectric properties by inducing and detecting nanoscale polarization changes. Utilizing a conductive tip to apply an external electric field induces a ferroelectric response, providing high sensitivity and spatial resolution for the direct observation and analysis of ferroelectric materials.

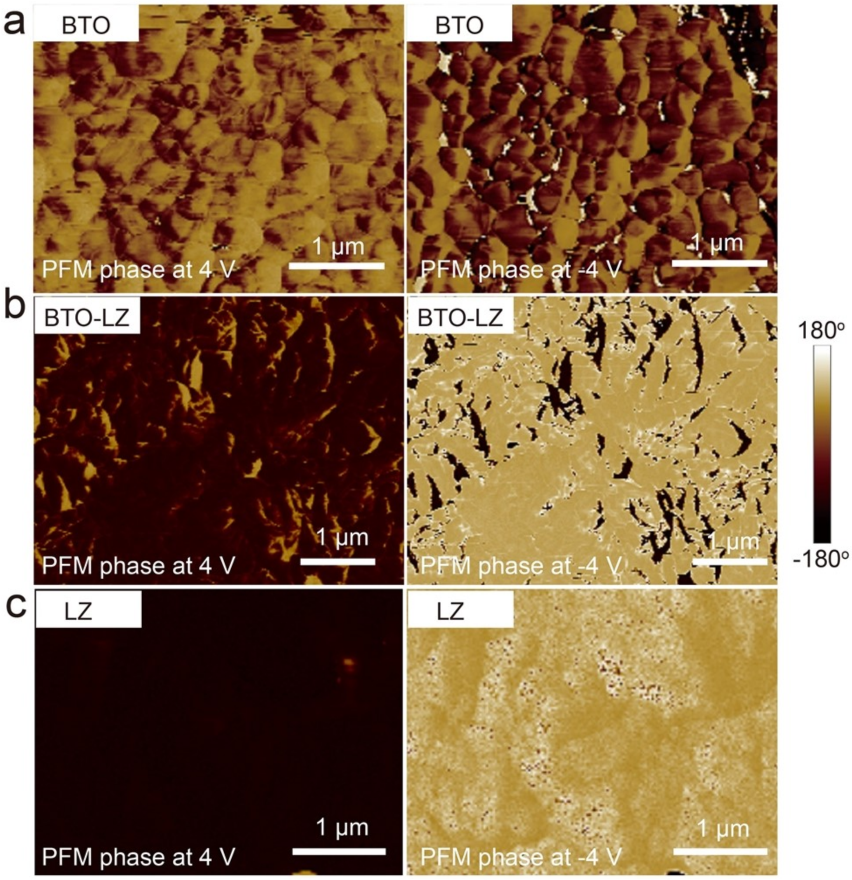

Fig. S9. The PFM phase of the (a) BTO, (b) BTO-LZ and (c) LZ at +4 V and -4 V bias voltage.

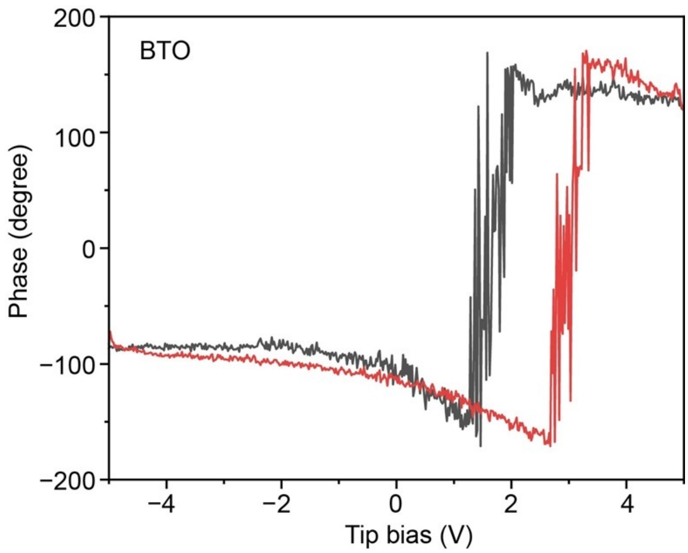

Fig. S10. Hysteresis loop obtained from piezoelectric force microscopy analysis of the BTO.

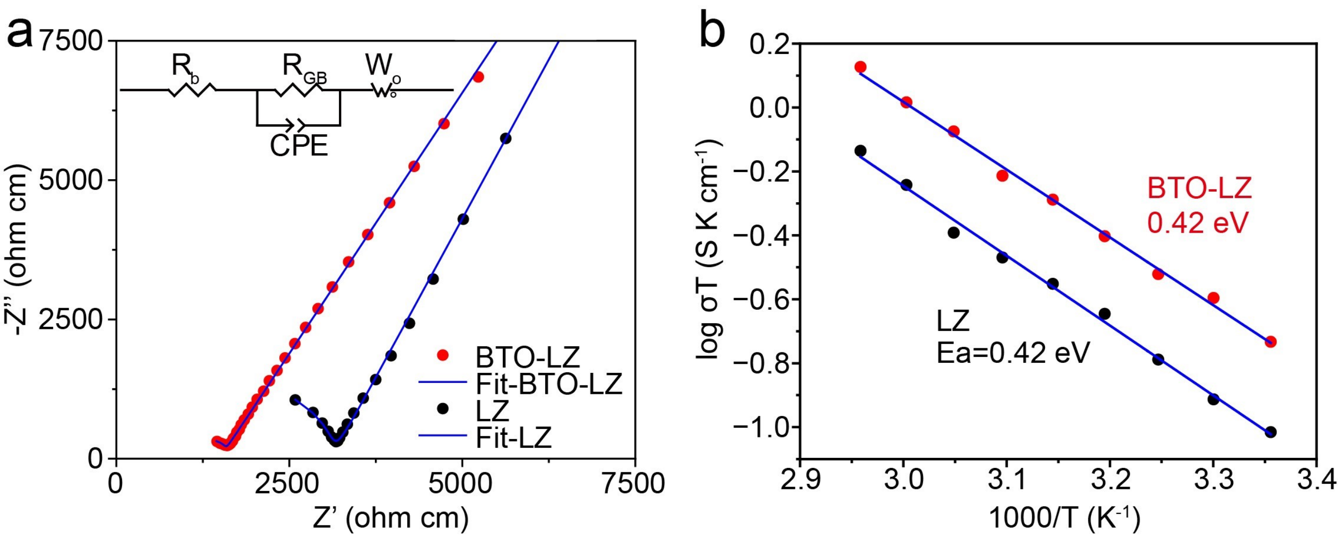

Fig. S11. (a) Ionic conductivities of the LZ and BTO-LZ pellets at 25 ^{o}C and (b) Arrhenius curves of the LZ and BTO-LZ pellets.

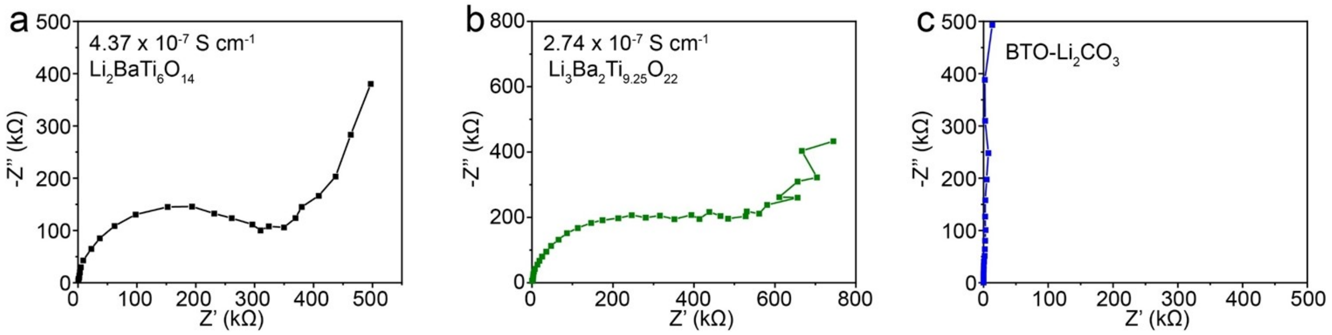

Fig. S12. Ionic conductivities of the (a) $Li_2BaTi_6O_{14}$, (b) $Li_3Ba_2Ti_{9.25}O_{22}$ and (c) BTO-Li_2CO_3 pellets at 25 °C.

Note: We prepared Li^+-doped BTO samples ($Li_2BaTi_6O_{14}$, $Li_3Ba_2Ti_{9.25}O_{22}$ and BTO-Li_2CO_3) using a conventional solid-state reaction method and tested their ionic conductivities. Specifically, $Li_2BaTi_6O_{14}$ or $Li_3Ba_2Ti_{9.25}O_{22}$ samples were prepared by weighing and ball-milling Li_2CO_3, BaO, and TiO_2 for 12 h. The resulting mixture was pressed into pellets and calcined at 1050 °C for 10 h in a muffle furnace. Additionally, BTO and Li_2CO_3 (7 wt%) were ball-milled for 12 h, pressed into pellets, and calcined at 1170 °C for 6 h.

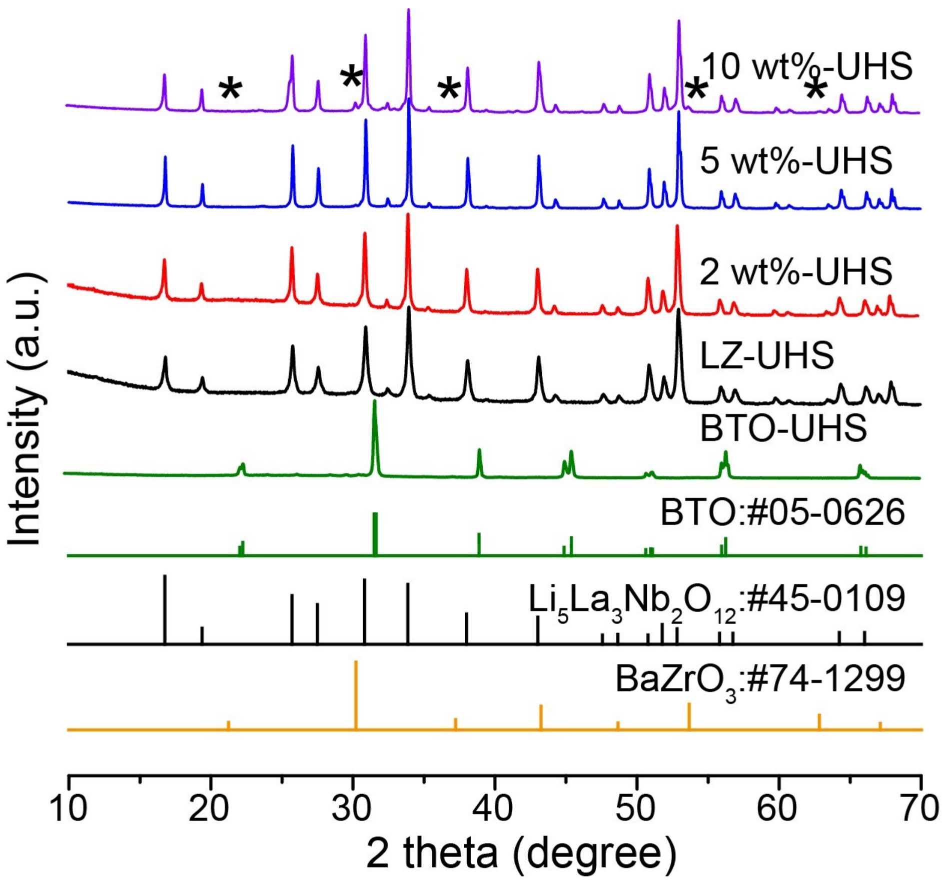

Fig. S13. XRD patterns of LZ-UHS, 2 wt%-UHS, 5 wt%-UHS, 10 wt%-UHS and BTO-UHS.

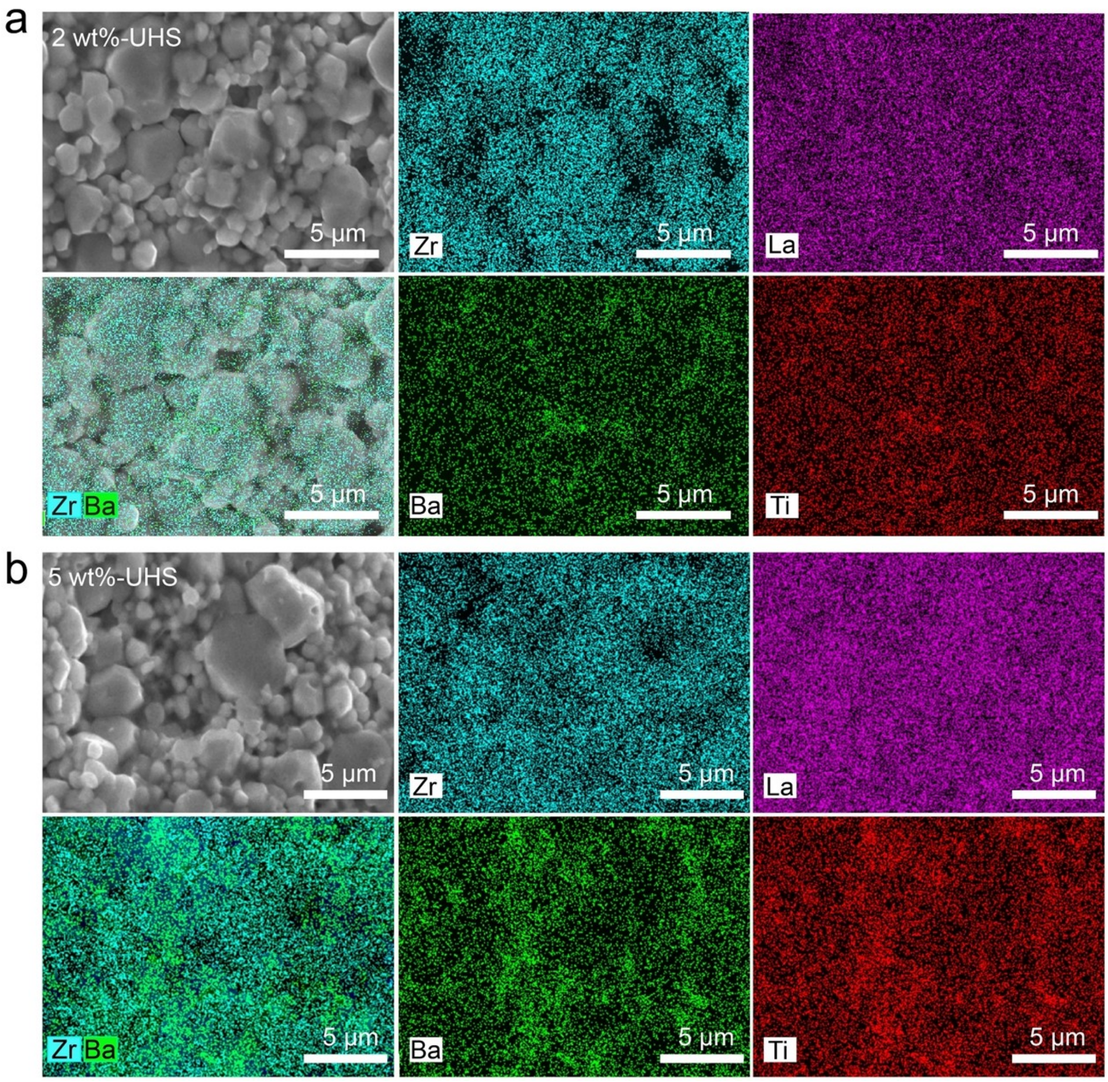

Fig. S14. Cross-sectional SEM images and EDS-mapping of (a) 2 wt%-UHS pellets and (b) 5 wt%-UHS**.**

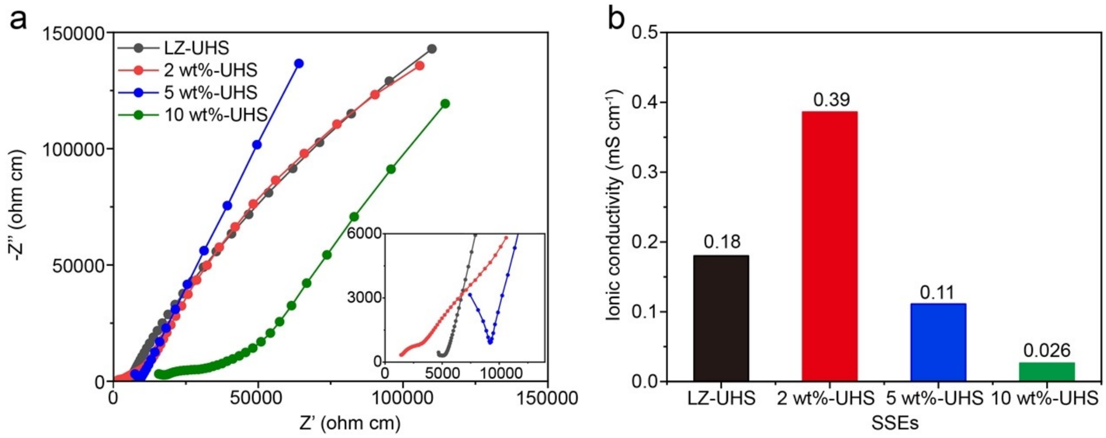

Fig. S15. (a) Normalized EIS curves and (b) ionic conductivities of LZ-UHS, 2 wt%-UHS, 5 wt%-UHS, 10 wt%-UHS.

Note: We also fitted the samples synthesized by the UHS, such as LZ-UHS, 2 wt%-UHS, 5 wt%-UHS and 10 wt%-UHS, to further understand the influence of the content of BTO. Notably, 2 wt%-UHS also shows a higher ionic conductivity of 0.39 mS cm^{-1} than the LZ-UHS of 0.18 mS cm^{-1}. In addition, with the increase of the BTO in the SSEs to 5 wt% and 10 wt%, the ionic conductivities are remarkably reduced.

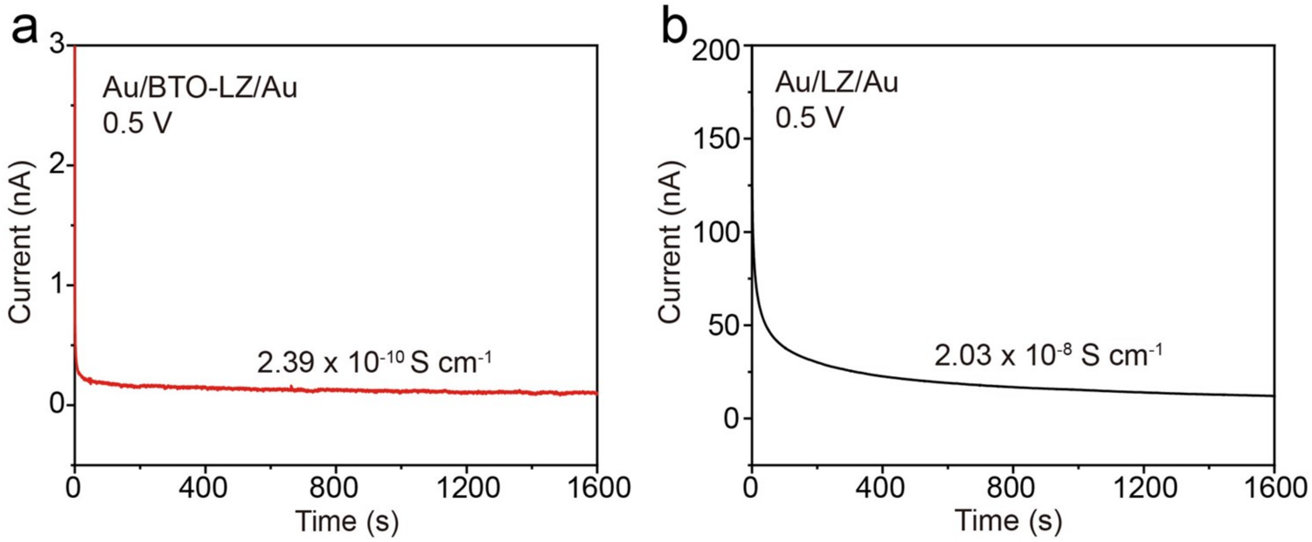

Fig. S16. Current-time curves of (a) the Au/BTO-LZ/Au cell and (b) the Au/LZ/Au cell under DC polarization at 0.5 V.

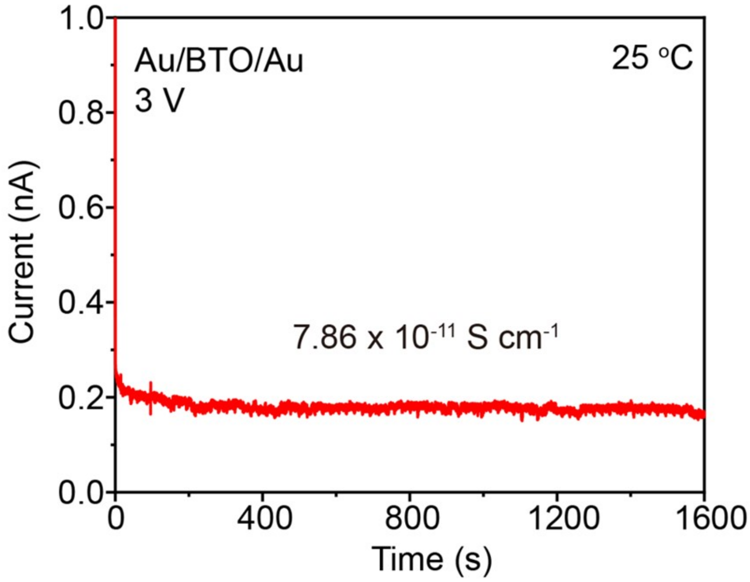

Fig. S17 Current-time curves of the Au/BTO/Au cell under DC polarization at 3 V.

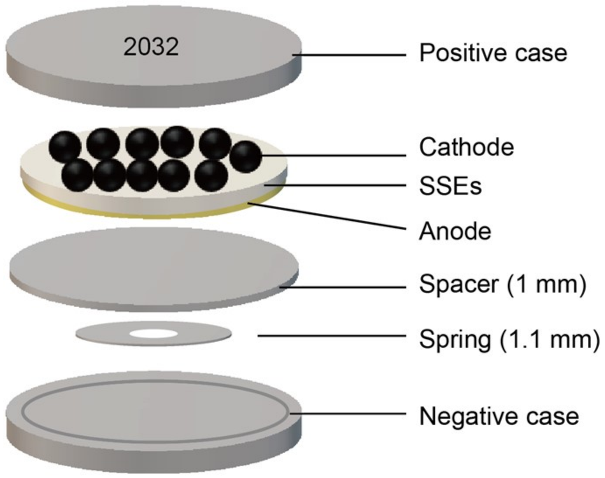

Fig. S18. Schematic of the cell stacked in a 2032-type coin cell.

Note: As shown in Fig. S18, the coin cell consists of the typical positive case, negative case, spacer (thickness: 1 mm) and spring (thickness: 1.1 mm). The pressure of the hydraulic crimping machine for assembling the coin cell was 500 PSI.

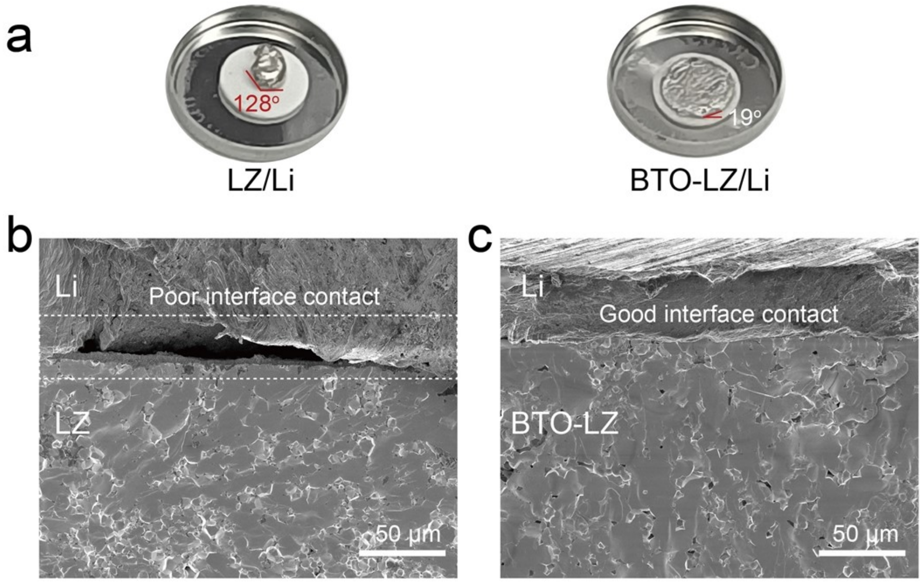

Fig. S19. (a) Optical photos of the wetting behaviors of molten Li on bare LZ and BTO-LZ. SEM images of (b) the LZ/Li interface and (c) the BTO-LZ/Li interface.

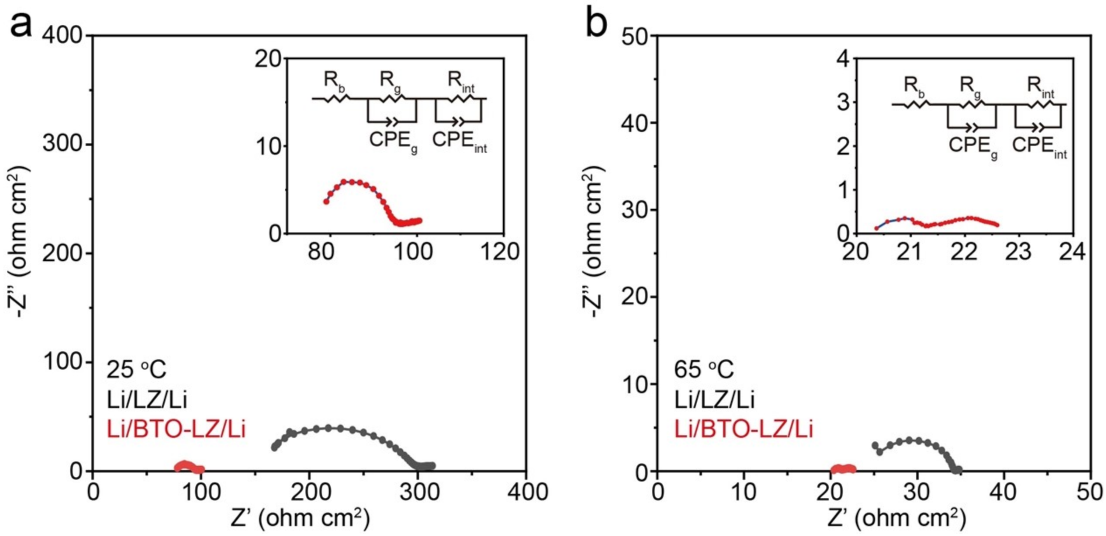

Fig. S20. ASR of Li/LZ/Li and Li/BTO-LZ/Li at (a) 25 °C and (b) 65 °C.

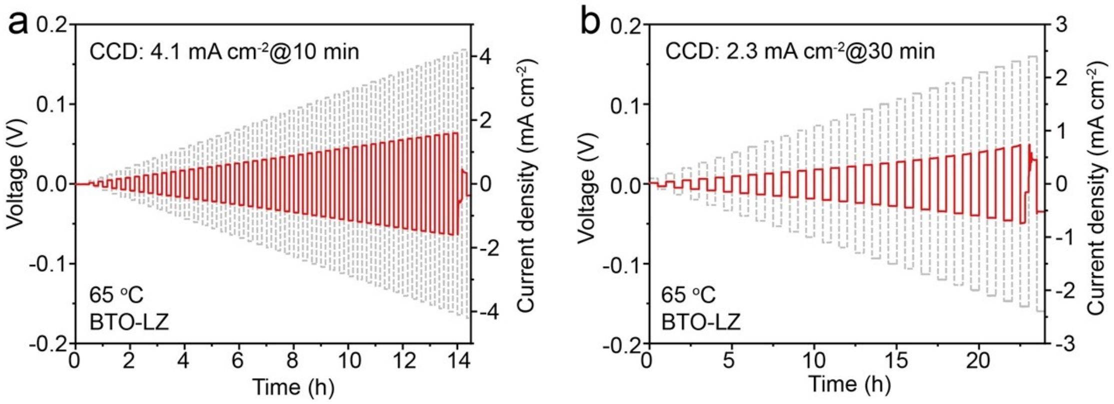

Fig. S21. CCD measurements of Li/BTO-LZ/Li with different capacities.

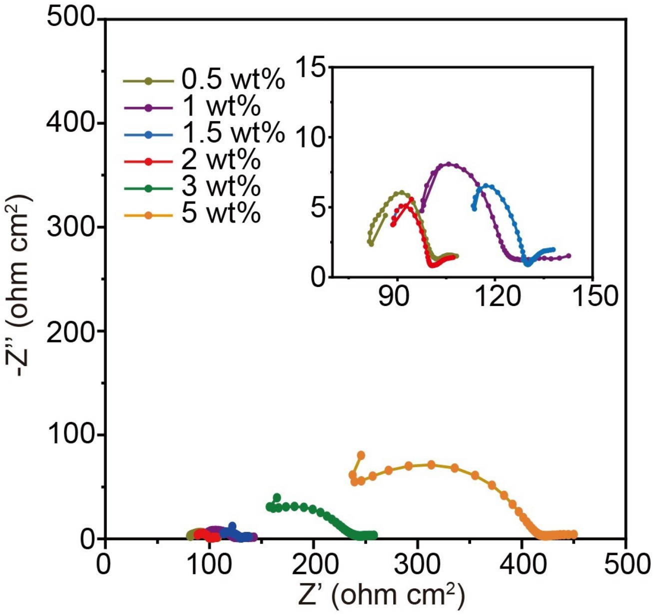

Fig. S22. EIS measurements of Li/BTO-LZ/Li with different weights of BTO.

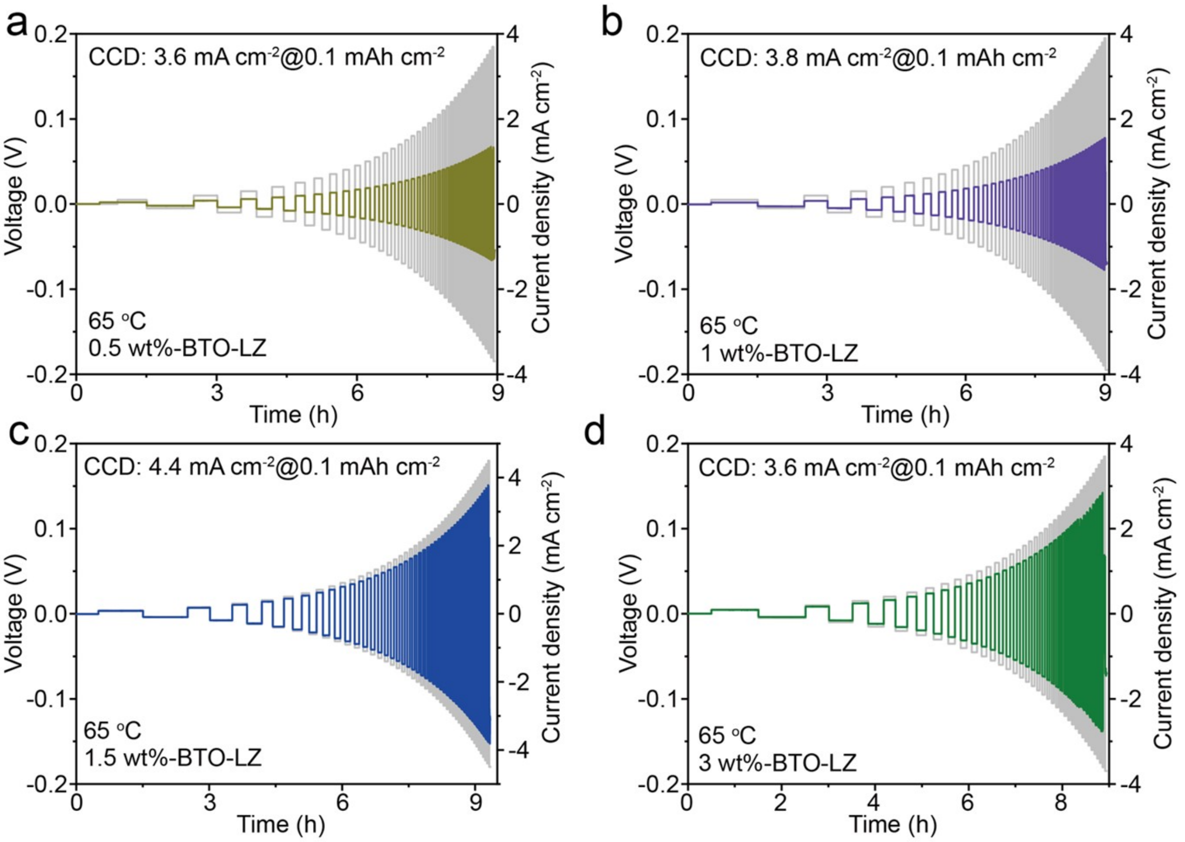

Fig. S23. CCD measurements of symmetric Li cells with (a) 0.5 wt%-BTO-LZ, (b) 1 wt%-BTO-LZ, (c) 1.5 wt%-BTO-LZ and (d) 3 wt%-BTO-LZ at 65 °C.

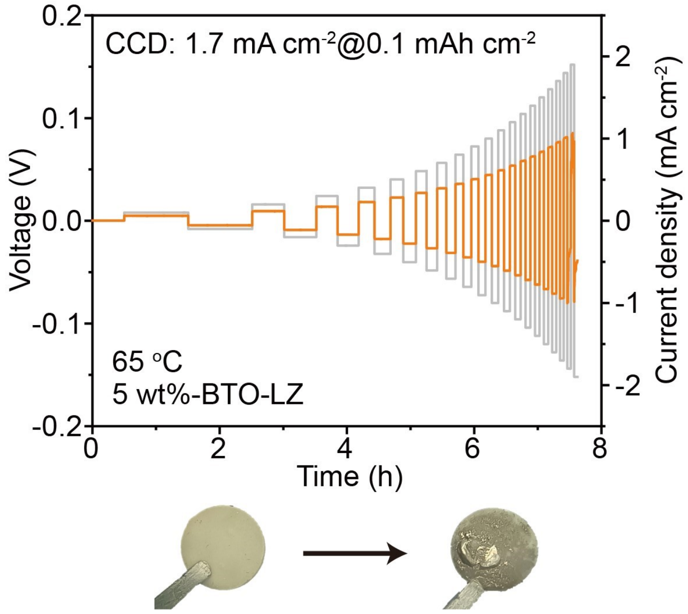

Fig. S24. CCD measurements of symmetric Li cells with 5 wt%-BTO-LZ at 65 °C and corresponding optical photos before and after contacting the molten Li.

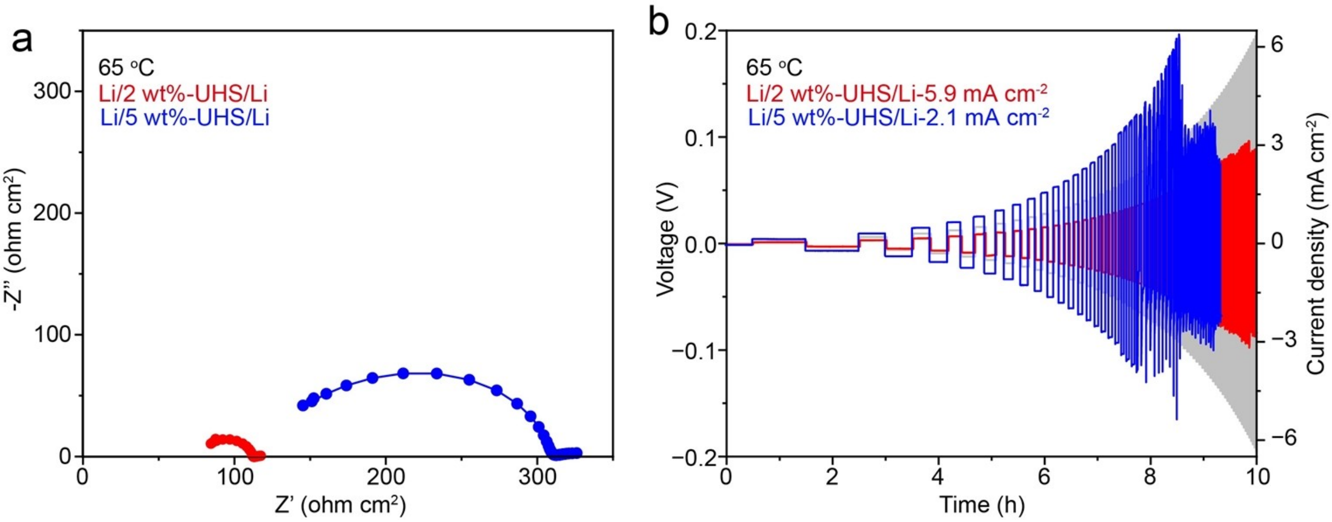

Fig. S25. (a) EIS measurements and (b) CCD measurements of 2 wt%-UHS and 5 wt%-UHS.

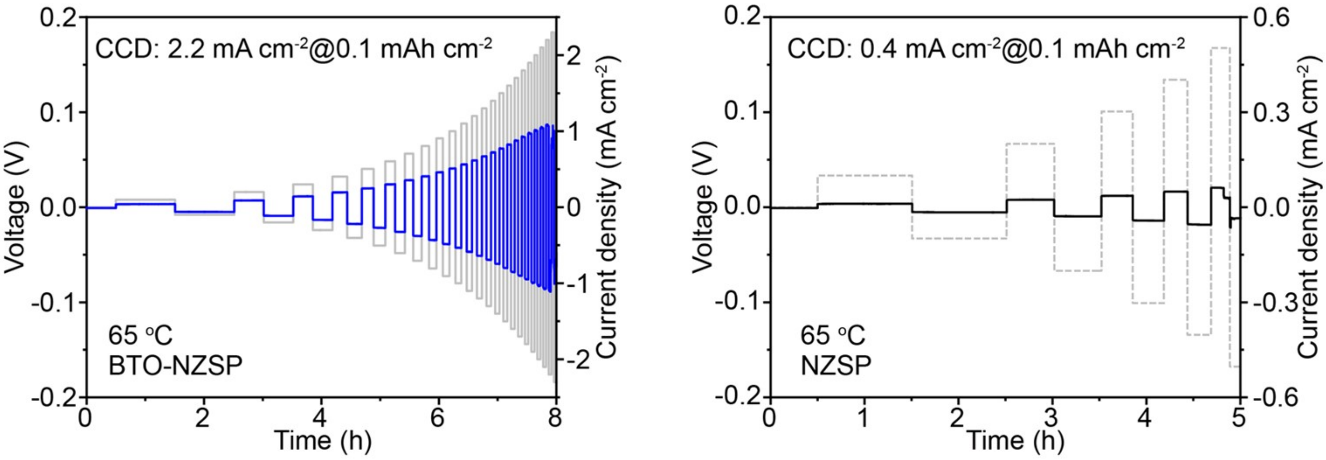

Fig. S26. CCD measurements of (a) Na/BTO-NZSP/Na and (b) Na/NZSP/Na at 65 ^{o}C.

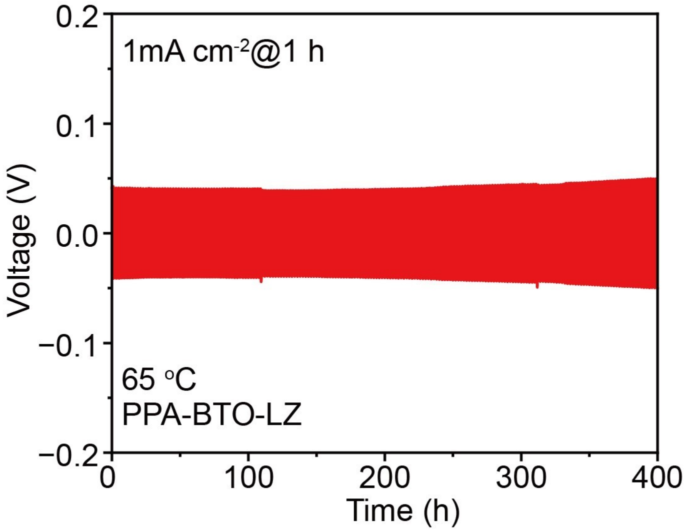

Fig. S27 Cycling performance of Li/PPA-BTO-LZ/Li at 65 °C at 1 mA cm^{-2} and 1 mAh cm^{-2}.

Note: PPA polymer was dissolved in DMSO solution by ultrasonic treatment. Then, BTO-LZ pellets were immersed into the PPA-DMSO solution (0.25% PAA in DMSO) for 2 h, followed by vacuum drying for 12 h at 110 °C.

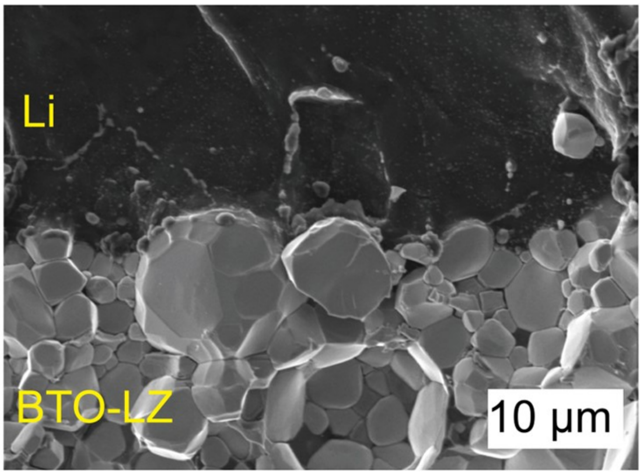

Fig. S28. Cross-section SEM images of a Li/BTO-LZ/Li cell after 100 hours at 1 mA cm^{-2}.

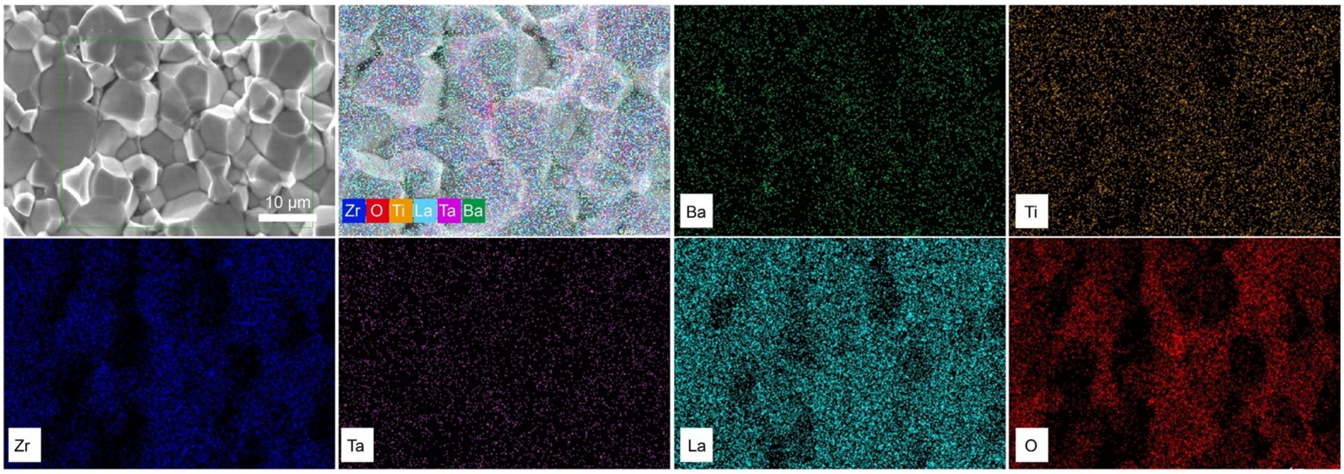

Fig. S29. EDS mappings of the BTO-LZ pellets after 100 h at 1 mA cm^{-2}.

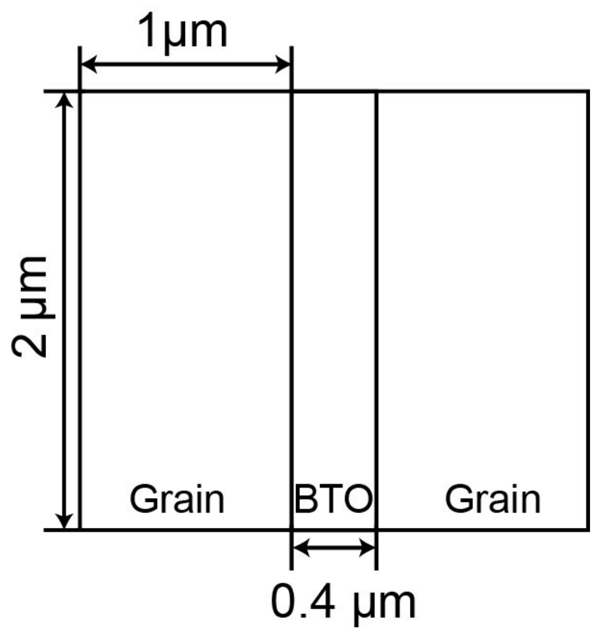

Fig. S30. Geometric model of the BTO-LZ in the COMSOL FEM analysis.

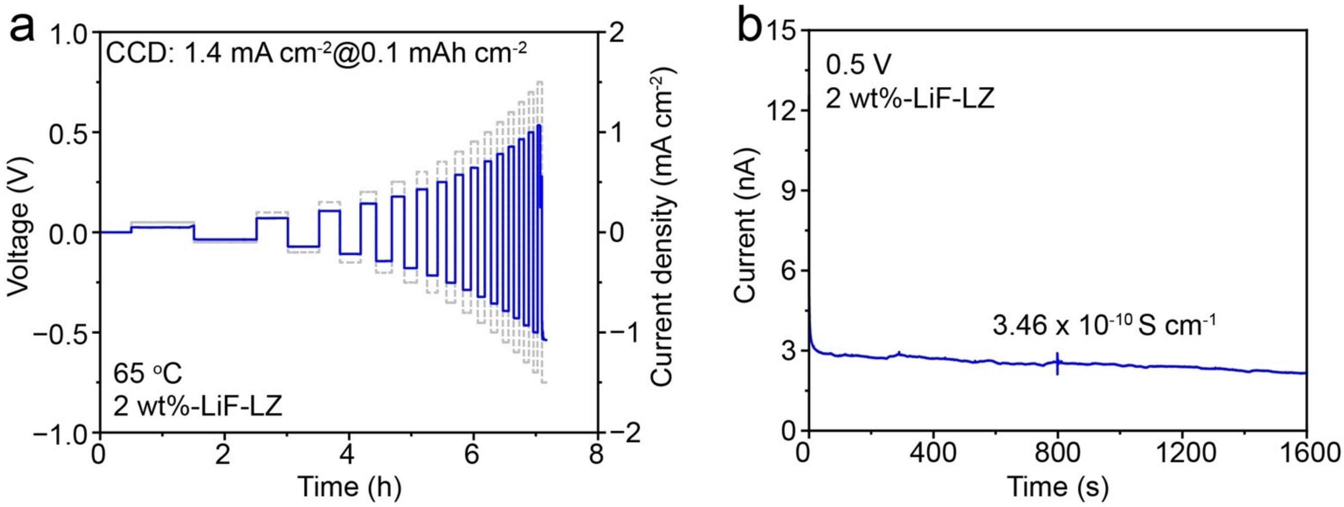

Fig. S31. (a) CCD measurements of Li/2 wt%-LiF-LZ/Li at 65 °C. (b) Current-time curves of the Au/2 wt%-LiF-LZ/Au cell under DC polarization at 0.5 V.

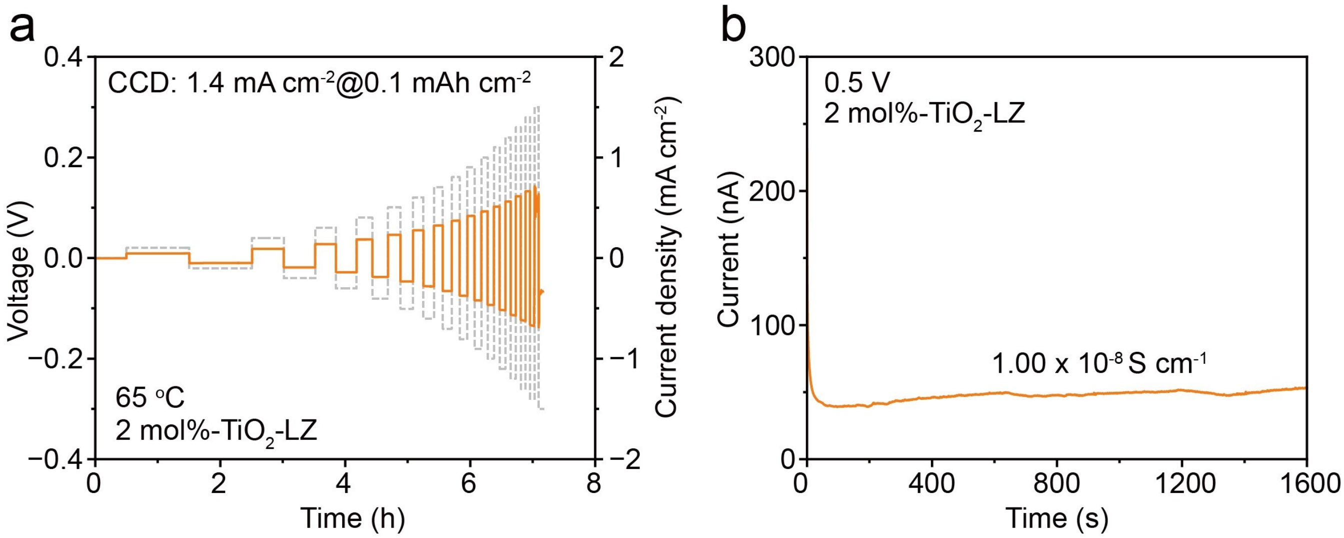

Fig. S32. (a) CCD measurements of Li/2 mol%-TiO_2-LZ/Li at 65 °C. (b) Current-time curves of the Au/2 mol%-TiO_2-LZ/Au cell under DC polarization at 0.5 V.

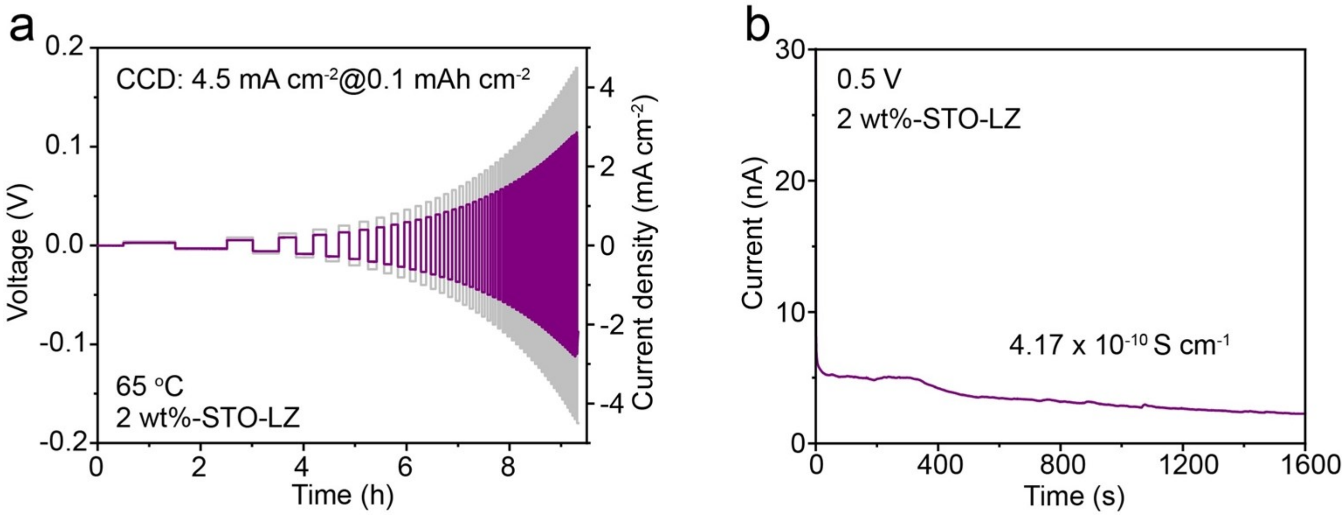

Fig. S33. (a) CCD measurements of Li/STO-LZ/Li at 65 ^{o}C. (b) Current-time curves of the Au/STO-LZ/Au cell under DC polarization at 0.5 V.

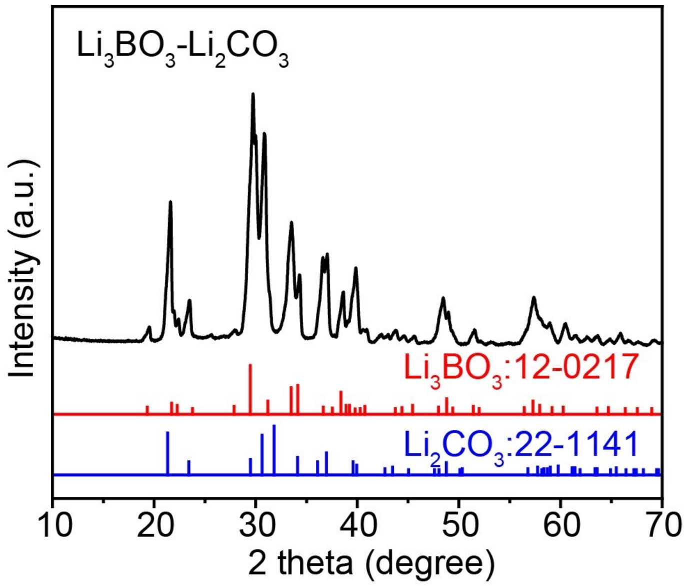

Fig. S34. XRD patterns of Li_3BO_3-Li_2CO_3.

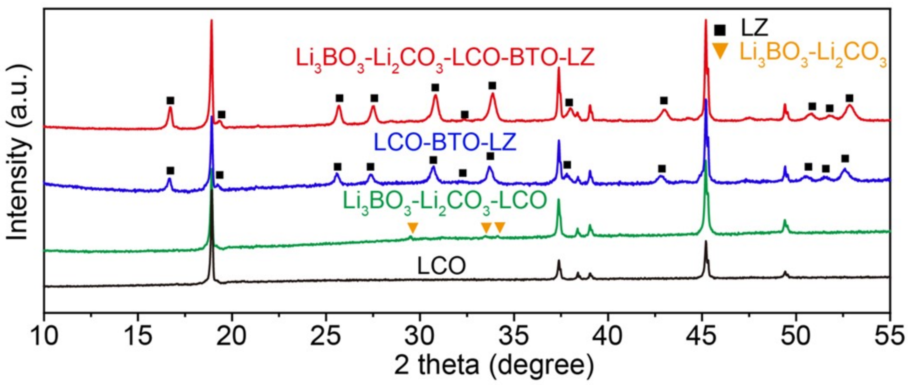

Fig. S35. XRD patterns of LCO, Li_3BO_3-Li_2CO_3-LCO, LCO-BTO-LZ and Li_3BO_3-Li_2CO_3-LCO-BTO-LZ.

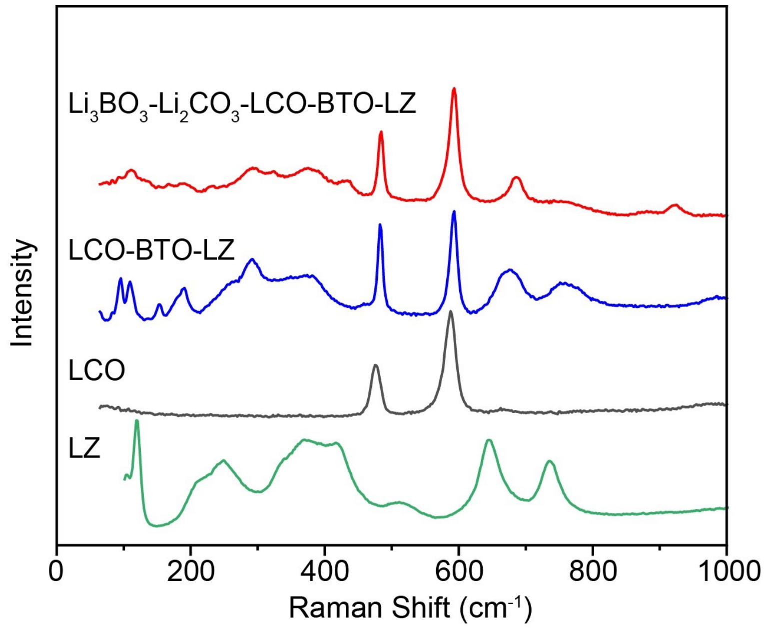

Fig. S36. Raman spectra of LCO, LZ, LCO-LZ and Li_3BO_3-Li_2CO_3-LCO-BTO-LZ.

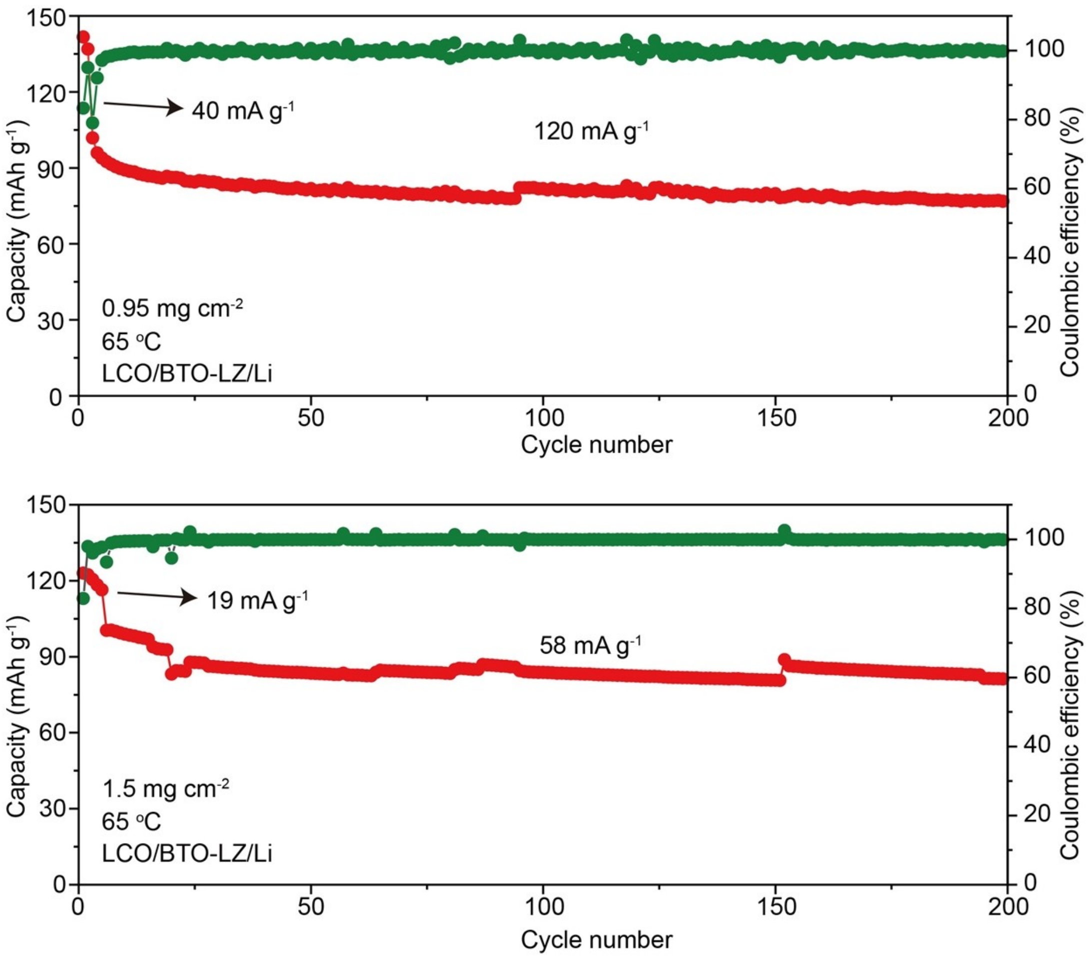

Fig. S37. Cycling performance and Coulombic efficiency of the LCO/BTO-LZ/Li ASSLBs at 65 ^{o}C.

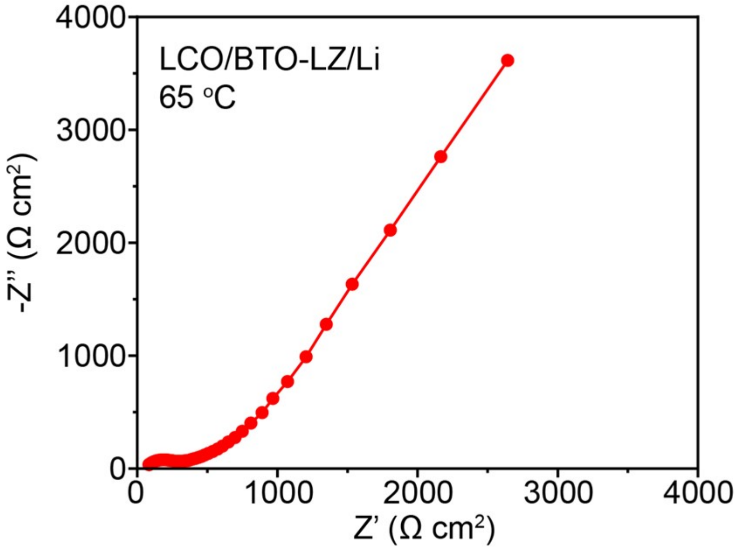

Fig. S38. EIS profiles of the LCO/BTO-LZ/Li full cells at 65 ^{o}C.

Table S1. The SSEs thickness and diameter, fitted resistance values, calculated ionic conductivity.

SSEs	R_b (ohm)	R_{GB} (ohm)	S/L (cm)	$\sigma_b Li^+$ (mS cm^{-1})	$\sigma_{GB} Li^+$ (mS cm^{-1})	$\sigma_{total} Li^+$ (mS cm^{-1})
LZ	115.8	451.5	5.49	1.57	0.40	0.32
BTO-LZ	85.66	178.2	5.81	2.01	0.97	0.65
LZ-UHS	212.5	297.7	10.89	0.43	0.31	0.18
2 wt%-UHS	127.7	161.1	8.98	0.87	0.69	0.39
5 wt%-UHS	144.3	492.3	14.02	0.49	0.14	0.11
10 wt%-UHS	608	2444	12.44	0.13	0.39	0.026

Table S2. CCD values comparison with previous literature for LLZO being above 1 mA cm^{-2} over 60 ^{o}C.

Modified method	Function	CCD (mA cm^{-2})	Ref
Al_2O_3	metallic interlayers	1.7	ACS Appl. Mater. Interfaces 2020, 12, 56118−56125.[1]
SnS_2	mixed-conducting interlayers (MCI)	1.2	ACS Appl. Energy Mater. 2021, 4, 2873-2880.[2]
Li-Naph	MCI	1.7	Adv. Sci. 2022, 9, 2105924.[3]
Glass-ceramic LZ	structural design	1.15	ACS Appl. Mater. Interfaces 2023,15, 28692−287.[4]
bilayer LZ	structural design	1.7	Cell Rep. Phys. Sci. 2023, 4, 101473.[5]
Ag-LZ	metallic interlayers	1.5	Sci. Adv.2022, 8, eabq0153.[6]
PPA	polymer-based Li^+ conducting interlayers	1.5	ACS Energy Lett. 2023, 8, 537−544.[7]
Ag-LiF-LZ	MCI	3.1	Sci. Adv.2022, 8, eabq0153.[6]
a-TPA-LZ	polymer-based Li^+ conducting interlayers	1.3	Adv. Funct. Mater.2023, 33, 2208013.[8]
CFx- LZ	polymer-based Li^+ conducting interlayers	3.2	Adv. Funct. Mater.2022, 32, 2208682.[9]
Li-Ga	metallic interlayers	1.7	Nat. Commun. 2020, 11, 3716.[10]
$LiCoO_2$-LZ	MCI	1.3	J. Energy Chem. 2023, 84, 181–188.[11]
Li_2S/Li_xSn-LZ	MCI	1.2	Nano Energy 2022, 91, 106643.[12]
Li-Na-LZ	metallic interlayers	2.1	ACS Energy Lett. 2020, 5, 1167−1176.[13]
Li_3N/Fe	MCI	3	Adv. Funct. Mater. 2021, 31, 2101556.[14]
LZO-LZ	Li^+ conducting interlayers	2	Chem. Eng. J. 2021, 411, 128508.[15, 16]
3D-ZnO-LZ	MCI	1.4	ACS Energy Lett. 2020, 5, 2156−2164.[17]
MoS_2	MCI	2.2	Energy Environ. Sci. 2019, 12, 1404-1412.[18]
NaH_2PO_2-LZ	MCI	2.6	Mater. Today 2022, 61, 65.[19]
BTO-LZ	Self-Polarized Ferroelectric Interphase, MCI	6.1	in this work

Table S3. Electrochemical performance of LLZO-based all-solid-state batteries.

Cathode Composition	Loading (mg cm^{-1})	T (°C)	Rate	Capacity (mAh g^{-1})	No. of Cycle(s)	Ref.
LCO + Li_3BO_3	1.7	25 °C,	0.05 C	85	5	20
LCO + porous LLZO scaffold	0.73	80 °C	0.05 C	118	14	21
LCO +Li_3BO_3+ In_2O_5Sn	1.2	RT	0.025	101	1	22
LCO@Li_2CO_3+ $Li_{2.3}C_{0.7}B_{0.3}O_3$ + LLZO@Li_2CO_3	1	100 °C	0.05 C	106	40	23
LCO + Li_3BO_3	/	/	0.01 C	78	1	24
LCO (PLD) + Li-Nb-O + LLZO	/		1 μA cm^{-2}	82	25	25
LCO + LLBZNO-LCO (UHS)	1	80 °C,	50 mA g^{-1} (0.3 C)	85	200	11
$Li_{2.985}B_{0.005}OCl$-LCO	1.85	90 °C	0.05 C	60	50	26
LCO-LBO-Li_2CO_3	**1**	**65 °C**	**143 mA g^{-1} (1 C)**	**83**	**200**	**This work**

SI References

1. Z. Huang, L. Chen, B. Huang, B. Xu, G. Shao, H. Wang, Y. Li and C.-A. Wang, *ACS Applied Mater. Interfaces*, 2020, **12**, 56118-56125.
2. D. Zhou, G.-X. Ren, N. Zhang, P.-F. Yu, H. Zhang, S. Zheng, Z.-W. Tian, S.-Y. Du, J.-X. Chen and X.-S. Liu, *ACS Appl. Energy Mater.*, 2021, **4**, 2873-2880.
3. B. Q. Xiong, S. Chen, X. Luo, Q. Nian, X. Zhan, C. Wang and X. Ren, *Adv. Sci.,* 2022, **9**, e2105924.
4. N. Hoinkis, J. Schuhmacher, T. Fuchs, S. Leukel, C. Loho, A. Roters, F. H. Richter and J. Janek, *ACS Appl. Mater. Interfaces,* 2023, **15**, 28692-28704.
5. H. Zhang, R. Dubey, M. Inniger, F. Okur, R. Wullich, A. Parrilli, D. T. Karabay, A. Neels, K. V. Kravchyk and M. V. Kovalenko, *Cell Rep. Phys. Sci.* 2023, **4**, 101473.
6. S. Lee, K.-s. Lee, S. Kim, K. Yoon, S. Han, M. H. Lee, Y. Ko, J. H. Noh, W. Kim and K. Kang, *Sci. Adv.*, 2022, **8**, eabq0153.
7. B.-Q. Xiong, Q. Nian, X. Zhao, Y. Chen, Y. Li, J. Jiang, S. Jiao, X. Zhan and X. Ren, *ACS Energy Lett.*, 2022, **8**, 537-544.
8. Y. Liu, J. Meng, M. Lei, Y. Yu, C. Lai and C. Li, *Adv. Funct. Mater.,* 2022, **33**, 2208013.
9. Q. Dai, J. Yao, C. Du, H. Ye, Z. Gao, J. Zhao, J. Chen, Y. Su, H. Li, X. Fu, J. Yan, D. Zhu, X. Zhang, M. Li, Z. Luo, H. Qiu, Q. Huang, L. Zhang, Y. Tang and J. Huang, *Adv. Funct. Mater.,* 2022, **32**, 2208682.
10. J. Meng, Y. Zhang, X. Zhou, M. Lei and C. Li, *Nat. Commun.*, 2020, **11**, 3716.
11. X. Liu, X. Kong, W. Xiang, Y. Jiang, B. Xiong, W. Ping, C. Xia, D. Huan and C. Wang, *J. Energy Chem.*, 2023, **84**, 181-188.
12. B. Zhao, W. Ma, B. Li, X. Hu, S. Lu, X. Liu, Y. Jiang and J. Zhang, *Nano Energy*, 2022, **91**, 106643.
13. Y. Zhang, J. Meng, K. Chen, H. Wu, J. Hu and C. Li, *ACS Energy Lett.*, 2020, **5**, 1167-1176.

14. M. Du, Y. Sun, B. Liu, B. Chen, K. Liao, R. Ran, R. Cai, W. Zhou and Z. Shao, *Adv. Funct. Mater.,* 2021, ***31*, *2101556***
15. Y. Ruan, Y. Lu, Y. Li, C. Zheng, J. Su, J. Jin, T. Xiu, Z. Song, M. E. Badding and Z. Wen, *Adv. Funct. Mater.,* 2020, **31**, 2007815.
16. C. Zheng, Y. Ruan, J. Su, Z. Song, T. Xiu, J. Jin, M. E. Badding and Z. Wen, *Chem. Eng. J.,* 2021, **411**, 128508.
17. H. Huo, J. Liang, N. Zhao, X. Li, X. Lin, Y. Zhao, K. Adair, R. Li, X. Guo and X. Sun, *ACS Energy Lett.*, 2020, **5**, 2156-2164.
18. J. Fu, P. Yu, N. Zhang, G. Ren, S. Zheng, W. Huang, X. Long, H. Li and X. Liu, *Energy Environ. Sci.,* 2019, **12**, 1404-1412.
19. Y. Liu, M. Lei, C. Lai, J. Meng, X. Wu, Y. Yu, Y. Zhang and C. Li, *Mater. Today*, 2022, **61**, 65-77.
20. S. Ohta, S. Komagata, J. Seki, T. Saeki, S. Morishita and T. Asaoka, *J. Power Sources*, 2013, **238**, 53-56.
21. K. J. Kim and J. L. M. Rupp, *Energy Environ. Sci.,* 2020, **13**, 4930-4945.
22. T. Liu, Y. Ren, Y. Shen, S.-X. Zhao, Y. Lin and C.-W. Nan, *J. Power Sources*, 2016, **324**, 349-357.
23. F. Han, J. Yue, C. Chen, N. Zhao, X. Fan, Z. Ma, T. Gao, F. Wang, X. Guo and C. Wang, *Joule*, 2018, **2**, 497-508.
24. S. Ohta, J. Seki, Y. Yagi, Y. Kihira, T. Tani and T. Asaoka, *J. Power Sources*, 2014, **265**, 40-44.
25. T. Kato, T. Hamanaka, K. Yamamoto, T. Hirayama, F. Sagane, M. Motoyama and Y. Iriyama, *J. Power Sources*, 2014, **260**, 292-298.
26. W. Feng, Z. Lai, X. Dong, P. Li, Y. Wang and Y. Xia, *iScience*, 2020, **23**, 101071.